

Photoluminescence of Fully Inorganic Colloidal Gold Nanocluster and Their Manipulation Using Surface Charge Effects

Anna R. Ziefuss, Torben Steenbock, Dominik Benner, Anton Plech, Jörg Göttlicher, Melissa Teubner, Benjamin Grimm-Lebsanft, Christoph Rehbock, Clothilde Comby-Zerbino, Rodolphe Antoine, David Amans, Indranath Chakraborty, Gabriel Bester, Milen Nachev, Bernd Sures, Michael Rübhausen, Wolfgang J. Parak, and Stephan Barcikowski*


Fully inorganic, colloidal gold nanoclusters (NCs) constitute a new class of nanomaterials that are clearly distinguishable from their commonly studied metal–organic ligand-capped counterparts. As their synthesis by chemical methods is challenging, details about their optical properties remain widely unknown. In this work, laser fragmentation in liquids is performed to produce fully inorganic and size-controlled colloidal gold NCs with monomodal particle size distributions and an fcc-like structure. Results reveal that these NCs exhibit highly pronounced photoluminescence with quantum yields of 2%. The emission behavior of small (2–2.5 nm) and ultrasmall (<1 nm) NCs is significantly different and dominated by either core- or surface-based emission states. It is further verified that emission intensities are a function of the surface charge density, which is easily controllable by the pH of the surrounding medium. This experimentally observed correlation between surface charge and photoluminescence emission intensity is confirmed by density functional theoretical simulations, demonstrating that fully inorganic NCs provide an appropriate material to bridge the gap between experimental and computational studies of NCs. The presented study deepens the understanding of electronic structures in fully inorganic colloidal gold NCs and how to systematically tune their optical properties via surface charge density and particle size.

1. Introduction

Noble metal nanoclusters (NCs), particularly those composed of Au, have attracted significant attention over the last two decades^[1,2] due to their photoluminescent properties. For instance, Au NCs exhibit small sizes and quantum yields (QY) several orders of magnitude higher than bulk gold,^[3,4] making them interesting candidates in bioimaging,^[4,5] sensing,^[6] catalysis,^[7,8] among other potential applications. In addition, Au NCs are highly interesting from a fundamental viewpoint as they bridge the gap between surface plasmon resonant nanoparticles (NPs) and quantized single atoms.^[1,9] In this context, it is important to differentiate between colloidal Au NCs synthesized in the presence of organic and inorganic ligands. Specifically, metal–organic compounds possess a very low Au-to-heteroatom ratio (e.g., for Au₂₅(SG)₁₈ with SG = glutathione, the

A. R. Ziefuss, Dr. C. Rehbock, Prof. S. Barcikowski
Technical Chemistry I and Center for Nanointegration
Duisburg-Essen (CENIDE)
University of Duisburg-Essen
Universitätsstraße 1-7, 45141 Essen, Germany
E-mail: Stephan.Barcikowski@uni-due.de

Dr. T. Steenbock, D. Benner, Prof. G. Bester
Department of Chemistry
Universität Hamburg
Institute for Physical Chemistry
Luruper Chaussee 149, HARBOR, Building 610
D-22761 Hamburg, Germany

 The ORCID identification number(s) for the author(s) of this article can be found under <https://doi.org/10.1002/adma.202101549>.

© 2021 The Authors. Advanced Materials published by Wiley-VCH GmbH. This is an open access article under the terms of the Creative Commons Attribution-NonCommercial License, which permits use, distribution and reproduction in any medium, provided the original work is properly cited and is not used for commercial purposes.

DOI: 10.1002/adma.202101549

Dr. A. Plech, Dr. J. Göttlicher
Institute for Photon Science and Synchrotron Radiation
Karlsruhe Institute of Technology
Hermann-von-Helmholtz-Platz 1
76344 Eggenstein-Leopoldshafen, Germany

M. Teubner, Dr. B. Grimm-Lebsanft, Prof. M. Rübhausen
Institut für Nanostruktur und Festkörperphysik
Center for Free Electron Laser Science (CFEL)
Universität Hamburg
Luruper Chaussee 149, 22761 Hamburg, Germany

M. Teubner
Department of Inorganic Chemistry
RWTH Aachen University
Landoltweg 1, 52074 Aachen, Germany

C. Comby-Zerbino, R. Antoine, Prof. D. Amans
Univ Lyon
Université Claude Bernard Lyon 1
CNRS
UMR5306
Institut Lumière Matière
Villeurbanne F-69100, France

ratio is 1:7,^[4] while fully inorganic Au NCs are electrostatically stabilized in liquid by adsorbed ions.

The vast majority of published studies address the photoluminescence of ligand-capped Au NCs.^[7,10,11] The findings remain diverse, and a multitude of different electronic processes seem to be involved. Thus, a clear distinction must be made between a few-atom NCs with particle sizes up to ≈ 1 nm and NCs in a size regime from ≈ 1 to 3 nm.^[10] The photoluminescence of few-atom clusters with known structures, especially Au₂₅(SR)₁₈, is relatively well understood, most likely attributed to the fact that these species can be synthesized with single atomic precision.^[4,12] In this case, photoluminescence could be clearly correlated to quantized electronic states of the core material involving interband (d–sp) and intraband (HOMO–LUMO) transitions with lifetimes in the nanosecond regime and constant Stokes shifts of ≈ 50 nm.^[13] The emission energy decreases with increasing NCs size,^[14] which is induced by decreased density of states, resulting in a smaller gap between the highest occupied and lowest unoccupied molecule orbital (HOMO and LUMO). However, the colloidal environment can also influence the photoluminescence properties.^[15,16] In the case of thiolate-capped Au NCs, visible as well as near infrared (NIR) emission with large Stokes shifts >100 nm occurs.^[17] Red to NIR emissions are attributed to a charge transfer from the thiolate ligand to the non-oxidized metal core. The quantum yield could be significantly increased by the application of electron donor moieties in the applied thiol ligands.^[15,16] Wu and Jin demonstrated that the photoluminescence of Au₂₅(SR)₁₈ NCs can be enhanced by increasing the donor ability of the surface ligands or the electropositivity of the metal core.^[15] Besides that, the nuclear charge, size of the NCs, and structure of the ligand are decisive for the QY. Moreover, Wang and co-workers found that the QY caused by lipoic acid ligands on the Au NCs depends on their oxidation state. The oxidation of sulfur bound to the gold surface leads to an increase in the quantum yield of the photoluminescence by up to 10%.^[18] In another case, photoluminescence emission was significantly blueshifted (0.1 eV) to the orange and yellow range when Au NCs were fabricated in the presence of glutathione.^[19] This phenomenon was attributed to the presence of abundant oxidized Au(I) species,^[20] which was considered to be a necessary prerequisite for photoluminescence in the observed system. Furthermore, photoluminescence was

occasionally observed in larger plasmon-resonant Au NPs, where a reduction of grain size on a single particle induced the parallel occurrence of red single-particle luminescence and plasmon resonance.^[21] Other studies observed blue photoluminescence in Au NPs, while particle size, surface oxidation, and predominantly surface ligands influenced the excitation and emission wavelengths and the luminescence intensity.^[22]

Contrarily, totally inorganic colloidal Au NCs have been sparsely studied, considering that they are difficult to fabricate by chemical synthesis routes, as organic ligands are required as reducing/etching agents and/or to produce sufficient colloidal stability. Note that it is impossible to quantitatively remove ligands, once they are on the colloidal particle surface.^[23] Pérez-Prieto and co-workers reported on a chemical reduction procedure of gold precursors in NaOH, yielding organic ligand-free, nonluminescent Au NCs.^[24] Contrarily, the group of Scaffardi and co-workers^[25,26] recently succeeded in producing organic ligand-free highly fluorescent few-atom Ag NCs using femtosecond-laser pulses ablating a solid target. The collected colloid includes a broad range of particle sizes that required a further mechanical centrifugation step to fractionate the few-atom NCs. The results revealed a broad photoluminescence after UV excitation, which could be explained by the large range of different sizes that were present in the plasmon-bleached colloids. Many questions about the origin of the photoluminescence of fully inorganic fluorescent colloidal NCs remain unanswered, especially the impact of surface charge density, due to the highly limited number of studies.

In this work, we fabricated inorganic NCs using laser fragmentation in liquids (LFL), which allows for the production of ultrasmall particles ($<<5$ nm) using ns-laser pulses applied to larger noble metal particles.^[27–29] In short, this process is based on the following principle. After a plasmonic Au NP absorbs photons from a laser pulse, hot electrons form and interact with the cold electrons of the conduction band via electron–electron scattering. Thermal equilibrium of the electron gas is reached in less than 100 fs, before electron–phonon coupling occurs within a few picoseconds.^[30] The heated lattice may lead to fragmentation, including phase explosion or Coulomb instability. If the laser pulse duration is longer than the characteristic times of the excitation and phase transitions, the reduction of particle size in the LFL process can be explained by a photothermal evaporation mechanism.^[27,29,31]

In advancement to previous works on LFL, we applied a purification strategy based on ultrafiltration to yield monomodal and monodisperse Au NCs, which, in the initial state, were only exposed to NaOH and NaCl. Based on these colloids that lack organic ligands, we studied the photoluminescence properties of different size regimes and experimentally evaluated the impact of surface charge density on the photoluminescence. Additionally, the density functional theory (DFT) and screened configuration interaction singles (SCIS) calculations were carried out to acquire a deeper understanding of the quantum mechanical processes that are induced by surface charges.

2. Results and Discussion

LFL provides a method to produce ultrasmall colloidal Au NCs without additional contribution of organic surface

Dr. I. Chakraborty, Prof. W. J. Parak
Department of Physics and Center for Hybrid Nanostructure (CHyN)
Universität Hamburg
Luruper Chaussee 149, 22761 Hamburg, Germany

Prof. G. Bester
Department of Physics
Universität Hamburg
Institut für Nanostruktur und Festkörperphysik
Luruper Chaussee 149, HARBOR, 22761 Hamburg, Germany

Dr. M. Nachev, Prof. B. Sures
Department of Aquatic Ecology and Centre for Water
and Environmental Research
University of Duisburg-Essen
Universitätsstraße 5, 45141 Essen, Germany

Prof. W. J. Parak
Department of Chemistry
Universität Hamburg
Grindelallee 117, 20146 Hamburg, Germany

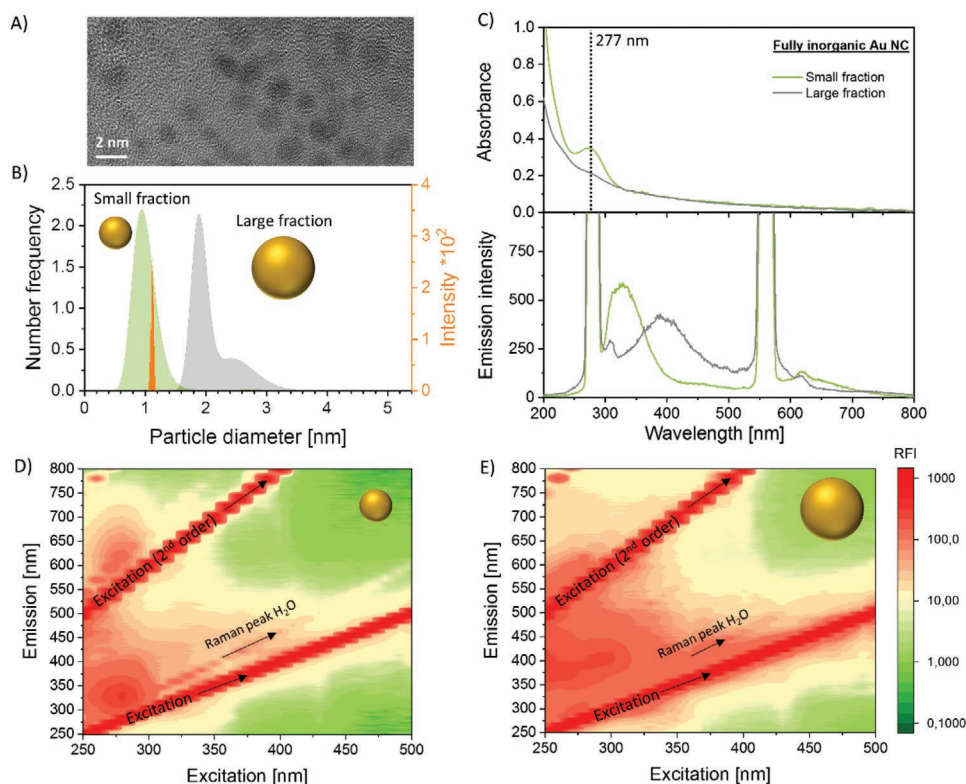


Figure 1. Photoluminescence of small and large, fully inorganic colloidal Au NCs. A) High-resolution transmission electron microscopy (HR-TEM) image of Au NCs after LFL and ultracentrifugation with a 50 kDa centrifugal filter. B) Number-weighted size distribution (measured with analytical ultracentrifugation (AUC)) after further ultracentrifugal steps with 3 kDa centrifugal filters (green, small fraction/gray, large fraction). Note that we additionally measured the smaller size fraction with ESI-MS (orange) (further information can be found in the Supporting Information). C) Absorbance spectra (top) and emission spectra (bottom, excitation 277 nm) after excitation of large and small Au NCs. D,E) 2D emission spectra of small (D) and large (E) Au NCs.

adsorbates. Although the produced colloid already contains Au NCs, a further size separation step is required in order to quantitatively remove plasmonic fractions. Scalfardi and co-workers^[25,26] employed mechanical centrifugation to produce inorganic Ag NCs; however, the resulting size distribution was rather broad, making it difficult to study the intrinsic particle properties in detail. In the present study, we used ultracentrifugation together with centrifugal filters containing a regenerated cellulose membrane for a more precise size separation (Figure 1). The use of filters with a molecular weight cut-off (MWCO) of 50 kDa was sufficient to quantitatively remove plasmonic NPs, leading to a colloid with particle sizes between 0.5 and 3 nm (Figure 1A; Figure S1, Supporting Information). Since the utilization of filters with a smaller MWCO allows for further size separation, we applied filters with a MWCO of 3 kDa and were able to produce a smaller size fraction (located in the filtrate) and larger size fraction (located in the retentate).

Our findings showing the disappearance of a gold surface plasmon resonance (SPR) peak in our size fraction between 0.5 and 3 nm are in fair agreement with findings from literature on ligand-capped Au NCs,^[32] though some deviations occur. Zhou et al. experimentally observed disappearance of SPR in particles smaller than 2.3 nm (Au₃₃₃) followed by a transition regime where neither plasmonic nor luminescence are observable,

followed by a particle diameter smaller 1.7 nm (Au₁₄₄), where distinctive emissions are dominant.^[33] Another study even suggests the occurrence of plasmon resonance for particles with average diameters of 1.3 nm, although these samples also contained significant amounts of particles >2 nm.^[34] Furthermore, these differences in the threshold diameter for SPR disappearance may also be attributed to different surface ligands and solvents used. It is yet unknown how the absence of organic surface adsorbates on Au NCs and high surface charge densities affect the size-dependent onset size threshold of SPR. In future, such ligand-free Au NC size series could be fabricated based on modified parameters within the fragmentation and centrifugation method established here.

The particle sizes were analyzed using analytical ultracentrifugation (AUC), and in the case of the smaller particles, electrospray ionization mass spectrometry (ESI-MS) was additionally employed. A narrow size distribution (Figure 1B) was found in each case. Note that particles were produced in ultrapure water without the addition of organic stabilizers. Therefore, one novelty of this study is that the optical properties of the Au NCs were investigated without any cross-effects caused by ligand-metal charge transfer (LMCT), which are induced by organic ligands. This allowed for a direct investigation of the surface charge density effects altered by the addition of inorganic surface adsorbates.

We observed a strong absorbance in the UV region (277 nm) for particles with mean diameters of 1 nm, which could not be detected for larger NCs with mean diameters of 2–2.5 nm (Figure 1C). This absorbance peak for particles smaller than 1 nm probably originates from the well-known onset of energy state quantization and, thus, a discretization of the energy levels.^[35] These findings are in qualitative accordance with the absorbance behavior of small ligand-capped Au NCs after wet-chemical synthesis,^[36] which supports that this absorbance is linked to the quantized energy state of the Au NC metal core. When both smaller particles (1 nm) and larger particles (2–2.5 nm) were optically excited by UV-light, a pronounced and clearly distinguishable photoluminescence could be detected (Figure 1C–E). The smaller size fraction was found to emit light between 300 and 350 nm and at ≈ 610 nm with a large Stokes shift, whereby the large fraction emitted light between 350 and 400 nm (peak maxima consideration). This observation clearly verifies that completely inorganic colloidal Au NCs can be fluorescent, which is still considered a controversial topic in literature.^[24–26] Quantum yield analysis of a colloid containing all cluster sizes between 0.5 and 3 nm (Figure S1, Supporting Information) indicated that 2% of all absorbed photons were emitted (measured at pH 8), which is 8 orders of magnitude higher than that for pure gold and in a comparable range to some studies of Au NCs in aqueous solutions bearing organic surface ligands.^[1,2,37] Even

though a QY of 2% can be considered moderate, it should be noted that this value was measured for a particle ensemble with sizes 0.5–3 nm and not on size selected fractions. Based on similar findings on ligand-capped Au NC,^[38] it may be anticipated that higher QY for optical applications could be possible for smaller particles, however, a systematic study on the QY-particle size-correlation was not the focus of this study.

In summary, we can state that the laser-generated fully inorganic Au NCs showed a pronounced photoluminescence, which differs between smaller and larger particle sizes. The particles free of organic ligands were produced through LFL followed by ultrafiltration. However, it is well known that Au NPs obtained from laser processing in liquids have partially oxidized particle surfaces, leading to a pH-dependent equilibrium of AuO^-/AuOH groups on the particle surface in aqueous solution,^[39–41] which can be varied through simple pH alteration.^[42] In the basic range, the AuO^- group is favored, which directly correlates with a better colloidal stability, as caused by electrostatic repulsion. Based on these findings, it may be concluded that the surface charge density of our Au NCs (derived from zeta potentials as specified by Makino and Ohshima^[43]) can be tuned by the pH value (Figure 2A; Figures S5–S7, Supporting Information). This gives the opportunity to correlate surface charge density with photoluminescence, which is systematically examined in the following paragraph.

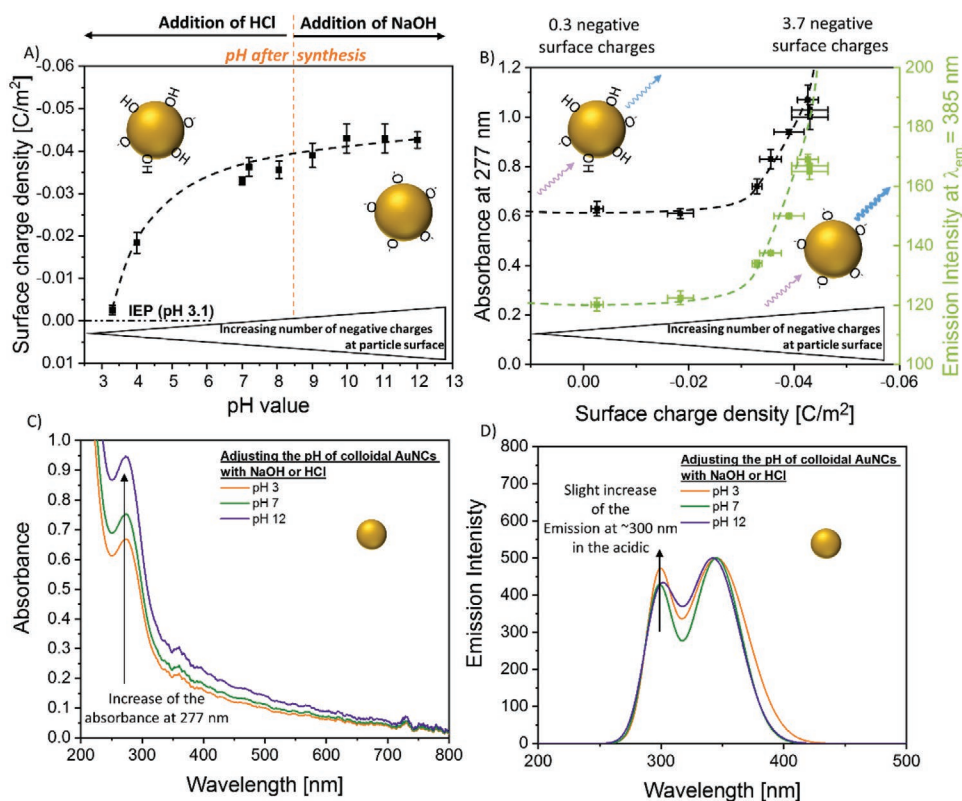


Figure 2. Surface charge density effects. A) Electronic and B) optical behavior of the large Au NC size fraction after the addition of NaOH and HCl. Absorbance was measured at 277 nm, emission intensity was measured at 385 nm after excitation at a wavelength of 277 nm. The inset sketches illustrate the increased emission intensity at high surface charge densities. C) Absorbance spectra and D) emission spectra of the small NC size fraction after pH adjustment. To exclude peaks associated with the excitation wavelength, we performed a multiple peak fit routine using a Gaussian peak function. The inset sketches in (C) and (D) remind that small particles are discussed within these graphics.

2.1. Influence of Ion-Induced Surface Charge Density on Photoluminescence

We experimentally investigated the effect of surface charge density on the large size fraction, as shown in Figure 1B in gray color. Here, NaOH and HCl were used to deprotonate and protonate surface-bound hydroxide groups (AuO^-/AuOH equilibrium), respectively, and to control the number of negative surface charges on the particles' surfaces.^[39,41] By varying the pH from the acidic to the strongly basic regime ($\text{pH} < 3$ was not achievable as particles aggregated), we observed a pronounced increase of the surface charge density with increasing pH (Figure 2A). Based on this, we calculated the number of elemental charges per Au NCs by normalizing the surface charge density by the surface area of one larger Au NC (2 nm) and the elemental charge. This yielded 0.3 to 3.7 elementary charges per particle (more information can be found in Section SII in the Supporting Information). Consecutively, we examined the optical properties of the corresponding particles at different pH values. We observed an increase in the broad absorbance band (200–600 nm) (Figure S6A, Supporting Information) with increasing number of negative charges. The increased absorbance was accompanied by an elevated emission intensity at 385 nm after excitation at 277 nm, while the emission wavelength at 385 nm remained constant (Figure 2B). To rule out side effects due to particle aggregation by pH alteration, which could also result in a decreased photoluminescence intensity^[44] or aggregation-induced emission,^[45] we checked the particle size distributions at different pH values using AUC and found no differences (Figure S7, Supporting Information).

Therefore, we can conclude that changes in photoluminescence intensity of larger Au NCs can be attributed to solvent effects influencing the surface charge density. Such effects have already been reported to influence the emission intensity, but were mostly studied in context with polarization of the solvent.^[46] We changed the polarization of the particles via deprotonation/protonation ($\text{OH}^-/\text{H}_3\text{O}^+$) and observed an emission intensity increase with increasing surface charge density. Note that the photophysical properties both at moderate and at significantly increased surface charge densities are long-term stable (see Section SII in the Supporting Information). Though not directly measured here, the increased fluorescence intensity with surface charge density might be a useful tool to increase the QY of the fully inorganic Au NC for applications. However, we did not aim at increasing the QY but want to strengthen the fundamental knowledge on the fluorescence origin in Au NCs.

Following Scanlon et al.,^[47] anion adsorption leads to a slightly positive particle surface, as excess electron density is transferred to the interior of the particle.^[47] This affects the local charge density of the surface, leading to an alteration of the surface potential.^[47] A partially electron-deprived (positive) surface would hence increase the absorption^[48] and the emission intensity, since reduced electronic density on the particle surface would decrease the probability of nonradiative transitions.^[49]

For the smaller Au NCs (Figure 2C,D), we observed an increase of the absorbance at 277 nm with the pH value, which seems to indicate similar charge-induced phenomena as those seen for the larger particles. The emission spectra, on the other hand, revealed a constant emission intensity at 350 nm,

while the higher energy emission at 300 nm increased when changing the medium to an acidic pH. However, the impact of the surface charge density on the optical properties of the smaller particles could not be determined experimentally, as colloiddally stable Au NCs in this size regime had concentrations too low for realistic zeta potential measurements, despite the charge states observed in nanoelectrospray ionization (nano-ESI)-MS being between 4 and 7 (see Figure S2 in the Supporting Information).

In order to explain the experimentally observed increase in the absorption intensity and to establish a relation between the emission behavior and the total surface charge in those small Au NCs, we performed DFT calculations for a series of $\text{Au}_{38}(\text{OH})_{24-x}(\text{O})_x^{x-}$ model particles ($X = 0, 2, 4$) differing in the total (negative) charge of the system obtained by abstracting protons from the hydroxy groups on the Au NC surface. As the Au_{38}NC core has a diameter of about 1 nm (8000 kDa), it closely matches the size regime determined experimentally (Figure 1; Figure S3, Supporting Information). The calculations were performed with aid of the wB97X-D range-separated hybrid exchange–correlation functional,^[50] the conductor-like screening model (COSMO)^[51,52] with parameters for water to simulate the solvent effects at the single-particle level, as well as a dhf-SVP-2c basis set,^[53,54] including spin–orbit effects (more computational details are given in the Supporting Information). We additionally performed SCIS calculations^[55] to obtain the excited state properties as a function of the total charge (or equivalently the degree of deprotonation). The obtained theoretical absorbance spectra (Figure 3A) are shown for three different charge states, i.e., 0, –2, and –4, which were chosen based on previous experiments on the larger particle size fraction (Figure 2B).

The calculated absorption spectra show one absorption band at 293 nm for the neutral structure (Figure 3A), which is in very good agreement with the absorption peak at 277 nm for the experimental spectra of small Au NCs (Figure 2C). Further, the experimentally observed increase in the absorption with increasing negative charge (or increasing degree of deprotonation) is well reproduced by the model system. While we found a blueshift of up to 10 nm for the negatively charged structures with respect to the neutral structure, this blueshift was noticeably smaller than the one obtained with DFT. This could potentially be a result of the basis set choice, which is assumed to be sufficient for neutral systems. Comparatively, anions ideally require basis sets with diffuse basis functions according to the literature,^[56] yet, no diffuse basis sets are currently available for spin–orbit calculations.

By analyzing the excited states with respect to their respective transition-dipole moments, we discovered that the 32nd excited state is strongly dominant for the neutral and twofold negatively charged structure. This dominant state corresponds to an exciton with dominant contributions from HOMO–2 and LUMO+2 (Table S1, Supporting Information). The varied intensity of the absorption peak from the 0 to –2 charge state can be tentatively explained by the observation that HOMO–2 and LUMO+2 tend to become more localized when the charges are added to the structure (Figures S9 and S10, Supporting Information). Furthermore, the much stronger increase of intensity when going from the –2 to –4 structures can be

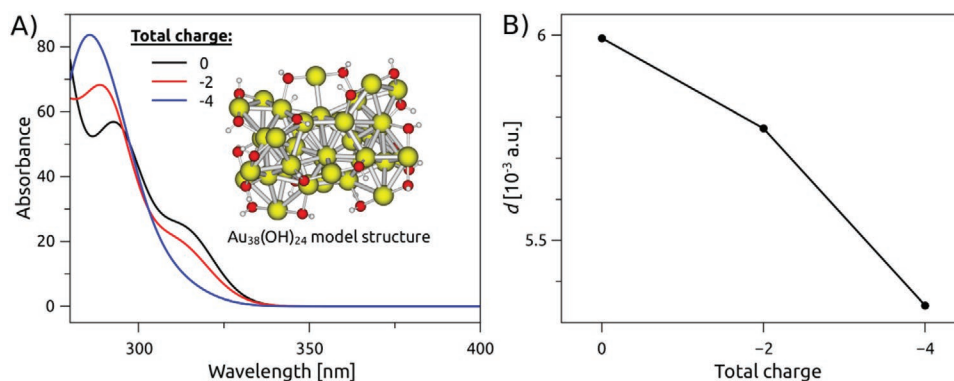


Figure 3. Calculated absorbance spectra depending on the degree of deprotonation (where we explicitly remove H^+ and thereby increase the size of negative total charges on the Au NC). A) Absorption spectrum calculated with SCIS and wB97X-D/dhf-SVP-2c/COSMO (water) employing a Gaussian broadening with a half width at half maximum of 120 meV. B) Transition-dipole moments of the lowest excitonic emitting state as a function of the total charge.

explained by the appearance of a second optical transition with large intensity for the -4 structure. This additional absorption peak mainly stems from a HOMO $-2 \rightarrow$ LUMO $+1$ excitation. When comparing the LUMO $+2$ with the LUMO $+1$, it can be deduced that both have very similar shapes in the -4 charged structures (see Figures S9 and S10 in the Supporting Information), which is then reflected in the emergence of a new bright HOMO $-2 \rightarrow$ LUMO $+1$ transition. The energetic difference between the transition energies of the two bright states in the -4 structure is only around 50 meV (see Table S1 in the Supporting Information) and cannot be resolved in Figure 3 due to the broadening.

Finally, the pH-dependent emission observed for the small Au NCs (Figure 2D) was approached by considering the lowest excited state as the emissive state, also known as Kasha's rule.^[57] It should be noted that this is a rather rough assumption because the exact kinetics of the emission process requires the study of the excited-state dynamics in these systems, which is out of the scope of this work. In agreement with experiment, we find that the transition-dipole moments d (the intensity is proportional to d squared) is decreasing with increasing negative total charge (Figure 3B). In all cases, the lowest exciton state is dominated by the HOMO \rightarrow LUMO single-particle states. By inspecting the shapes of the HOMO and LUMO (Figure S10 and S11, Supporting Information), it can be seen that when the negative charge is increased, the HOMO shows larger contributions from the deprotonated oxygen atoms on the surface, while the LUMO becomes more localized on the gold core. Consequently, the overlap of the HOMO–LUMO decreases, resulting in lower transition-dipole moments with respect to the charge.

Summarizing the experimental results in the surface anion adsorbate effects: the fully inorganic particles with a mean size of 1 and 2–2.5 nm react differently to altered surface charge densities. While both species show an increased absorbance behavior with increasing negative charges around 277 nm, an optical excitation at this wavelength leads to an increased emission intensity for the larger Au NCs, which cannot be observed for the smaller Au NCs. The latter, however, show a decrease of the emission intensity around 300 nm, verified by DFT and SCIS calculation (Figure 3B). For both sizes, the observed changes in the emission intensity are influenced by

the increased surface charge density (with opposite trends for both size regimes) while no influence on the emission energy could be observed. It indicates that the gold (surface) lattice structure of the particles is not changed by the addition of inorganic additives.

However, irrespective of the surface charge density influence, the absorbance and emission behavior of the two studied size fractions (1 nm vs 2–2.5 nm) of totally inorganic Au NCs was fundamentally different. This could originate from I) a difference in the crystal structures, or II) a change in the quantization of energy states. A detailed investigation of these two effects in inorganic Au NCs as well as their interplay is documented in the following paragraphs.

2.2. Structural Resolution of Larger and Smaller NCs

To study the lattice structure of Au NCs, we utilized X-ray absorption spectroscopy (XAS), including X-ray absorption near edge structure (XANES) and extended X-ray absorption fine structure (EXAFS). The averaged gold valency can be deduced from the XANES spectrum (Figure 4A). While monovalent gold shows a spectrum very similar to metallic (fcc) gold, trivalent gold exhibits a marked difference with a distinct peak around 11.92 keV that can be modified by the amount of charge transfer when coordinated with chlorine, bromine, or water.^[58] Fits of the XANES spectra for both size distributions (1 nm vs 2–2.5 nm) reveal that a fraction of 30–35% for <1 nm Au NCs and 20–30% for >1 nm may be oxidized. However, the portion of Au(I) could not be determined with sufficient accuracy due to the similarity of the spectrum to metallic gold. The atomic correlation as derived from EXAFS is surprisingly similar for both the NCs samples and metallic gold (Figure 4B). Therefore, we conclude that even the small-sized fraction shows an fcc-like local order seen at the expected atomic distances of 2.88 and 4.08 nm (Figure S17, Supporting Information). The correlation for larger distances is naturally dampened due to the finite size of the clusters and possibly some disorder.

The results also interestingly reveal that even the smaller Au NCs (consisting of about 40 gold atoms) exhibit a pronounced fcc-like structure similar to bulk gold, while the more

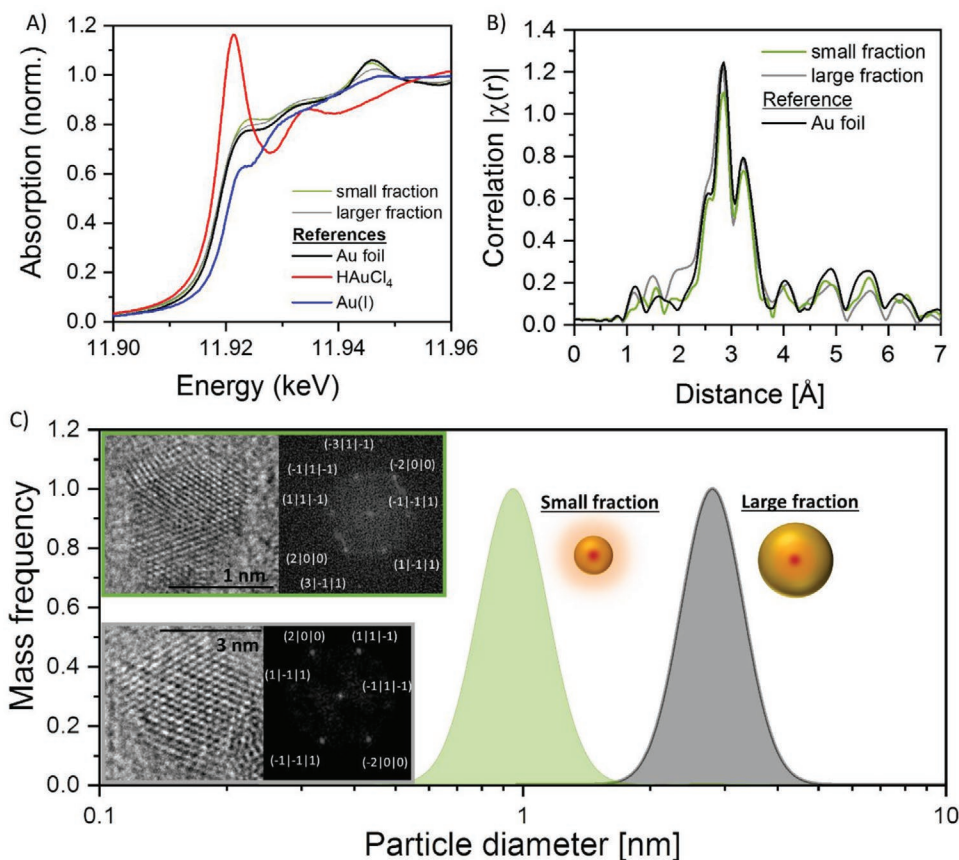


Figure 4. Structural characterization. A,B) Results from XAS measurements with: A) the XANES part around the L(III) absorption edge of both NC size fractions as well as references of a gold foil, aqueous HAuCl_4 , and reduced Au(I) stabilized by CTAB and B) Fourier transform $\chi(r)$ of the cube weighted oscillation $\chi(k)$ extracted from the EXAFS signal for both size fractions as well as the gold foil. C) Ultracentrifuge-fractionated particle size distributions with HR-TEM images and Fourier transforms as inset. Both particles are in a $[011]$ zone axis.

frequently discussed metal–organic compounds with thiolated ligands have very unique crystal structures.^[59] Note that XAS is not a surface sensitive technique. In addition, surface defects could contribute to the optical properties of Au NCs and are expected as the laser-based synthesis technique involves an extremely fast cooling of the vaporized material and can freeze metastable crystal structures.^[29,30] To probe more sensitively for potential surface defects, we performed high-resolution transmission electron microscopy (HR-TEM) measurements with consecutive image analysis. In accordance with the EXAFS, we found a global fcc-like structure (Figure 4B; Figure S17, Supporting Information). A more detailed examination of the HR-TEM images (Figure 4C; Figure S14, Supporting Information) reveals a more frequent occurrence of $(3|1|1)$ crystal facets in the smaller Au NCs. This seems to indicate that the surface of the small-sized fraction Au NCs is more distorted and causes one crystal facet to preferentially adsorb on the TEM grid (statistic evaluation can be found in Figure S12 in the Supporting Information).

In the previous paragraphs, we concentrated on the observation of two Au NC colloids with clearly distinguishable, non-overlapping particle size distributions. In the subsequent experiments, we used adapted particle size separation techniques to systematically elucidate whether there is a clear particle size

effect on the optical properties of the fully inorganic Au NCs and whether we can use the findings to deduce a quantum-size effect.

2.3. Elucidation of Quantum-Size Effects in Fully Inorganic Colloidal Au NCs

We measured the emission of 17 different monodisperse, but not atomically precise, gold nanocluster colloids after excitation at 275 nm. A total of six different emission wavelengths were obtained (Figure 5A; Figures S15 and S16, Supporting Information), which varied in occurrence and intensities with particle size. The most frequently occurring emission peak was located between 350 and 400 nm, which can be observed for all particle sizes. An increased particle size resulted in a redshift of the measured emission. A comparable behavior of organometallic gold clusters was previously reported in the literature.^[17,60] By reducing the number of atoms in precise clusters, the energy of the emission will increase, which can be explained by the decreasing particle volume, inducing a larger optical bandgap. Based on these findings, we conclude that the origin of this emission is probably related to the particle core. Besides, we measured the lifetime of 1.1 nm particles, which show a core emission around 340 nm (for

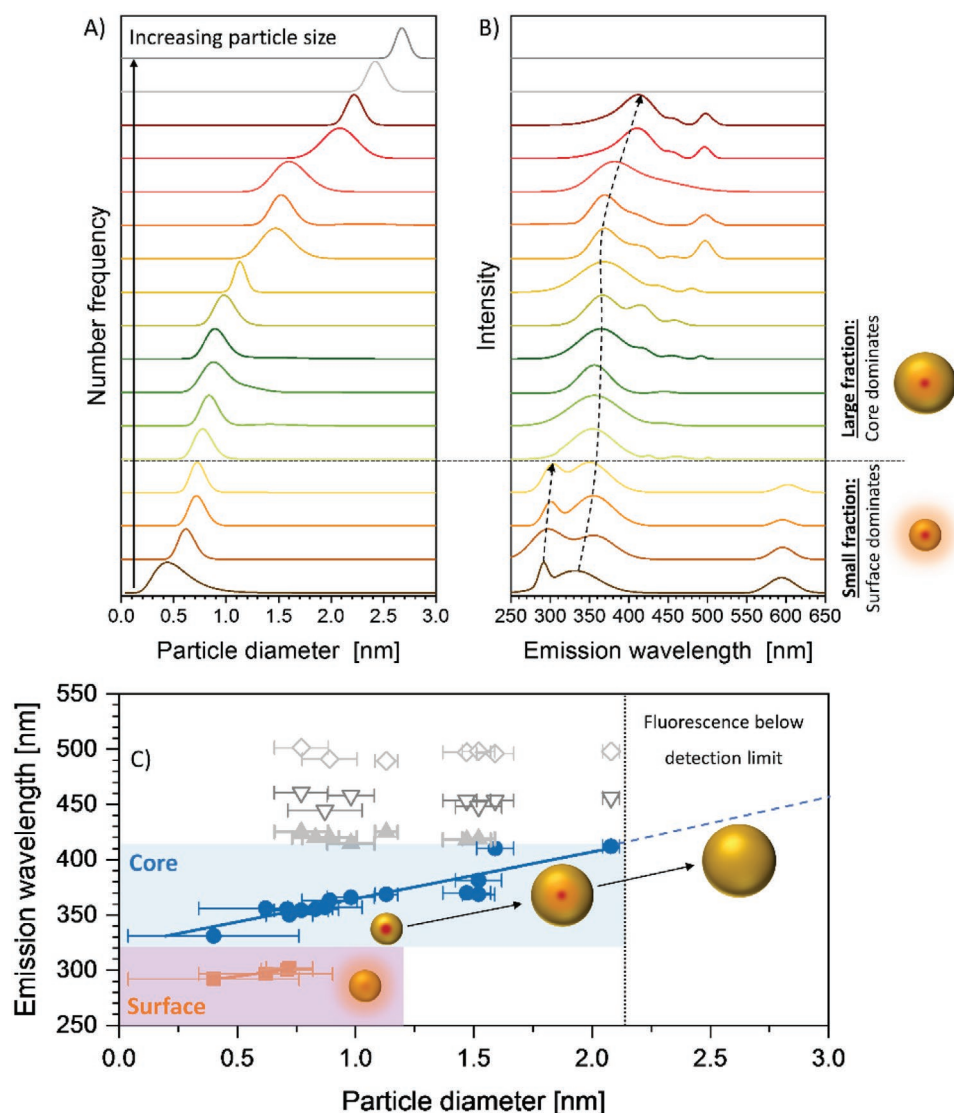


Figure 5. Particle surface and core contribution to the photoluminescence of fully inorganic Au NCs: A) Number-weighted size distribution of the investigated samples as obtained by AUC measurements. B) Emission spectra after excitation at 275 nm using the same color code as in (A). C) Position of the emission wavelength after excitation with 275 nm as function of mean particle diameter. The individual contribution of surface states (orange) and core states (blue) can be influenced by particle size. The additional emission wavelengths are indicated in gray.

further description, see Section SVI in the Supporting Information). The decay profiles (Figure S18C, Supporting Information) can be fitted with a triexponential decay, which gives lifetimes of 2.20 ± 0.01 ns (60.5%), 1.01 ± 0.01 ns (36.1%), and 0.09 ± 0.01 ns (3.4%). Such small lifetimes were expected as longer lifetimes primarily correlate with a ligand–metal charge transfer in ligand-capped Au NC systems.^[38]

Further dominant emission peaks were found at 300 and 610 nm and were only visible for particles smaller than 1 nm (Figure 5B,C). The main characteristic of these smaller particles is that their specific surface area in the colloid was large. Basic calculations of these smaller particles, assuming sphericity, indicate that the majority of atoms are located at the interface to the dispersion medium. Based on these findings, we hypothesize that these emission features are connected to surface states and could be further linked to the occurrence of a structural

surface deformation, as indicated by the HR-TEM measurements. It is well known that the presence of surface defects coincides with distinctive surface features, which can influence electron–phonon coupling and energy relaxation.^[61] Such defects could be responsible for the occurrence or amplification of these surface state emission lines. As already mentioned, three other emission wavelengths (420, 450, and 490 nm) were detected, but only contribute significantly for particle diameters larger than 0.7 nm. The wavelength of these contributions showed no size dependence.

A compilation of all spectra can be found in Figure 4C, where only Au NCs in the size range 0.5–2.2 nm show emission, thus the occurrence and energies are dependent on the particle size. While core-emission was energetically sliced off, the surface emission possessed the largest bandgap, indicating a high-energy emission or small Stokes shift to the excitation.

3. Conclusion

Fully inorganic, colloidal NCs are an underexplored new class of nanomaterials that allow the investigation of surface charge effects on the optical properties, excluding ligand–metal charge transfer effects from organic molecules. Such inorganic Au NCs are accessible through pulsed laser fragmentation in liquids and size-controlled via fractionation procedures. They exhibit pronounced photoluminescence even in the absence of organic ligands with quantum yields comparable to those of their ligand-capped counterparts. Herein, we demonstrated that their emission behavior is size-dependent and dominated by core state emission for larger particles (2–2.5 nm) and by surface state emission for smaller particles (<1 nm). Within this fundamentally based study, we found that their emission intensity is a direct function of the surface charge density and is easily controllable by the pH of the surrounding medium. While the deprotonation of hydroxide groups on the larger NCs leads to an increase of the emission, the same leads to hardly any effect with the small particles' core emissions. However, we observe a small decrease of the more energy-rich surface emission. To explain this effect, we have performed supporting DFT simulations on an $\text{Au}_{38}(\text{OH})_{24-x}(\text{O})_x^{x-}$ model particle. The theoretical insight allows an explicit explanation of this observation. It shows that the HOMO is dominated by contributions from the deprotonated hydroxide at the particles surface, whereas the LUMO is localized closer to the particles' core. The overlap of both decreases, resulting in the lower experimentally observed surface emission intensity. These findings not only deepen our understanding of the origin of photoluminescence in Au NCs, but they also reveal that core state emission from metal atoms is a major contributor to the photoluminescence in Au NCs. The latter phenomenon has only been predicted by theory until now—this work experimentally verifies that an overlap with organometallic charge transfer bands in chemically generated NCs could be responsible for the photoluminescence. Hence, fully inorganic NCs are an excellent model to bridge the gap between theory and experiment. Furthermore, our results stress the importance of surface-dominated emission states, which emerge even in the absence of organic surface adsorbates and become particularly dominant for particles <1 nm. Another interesting finding is the direct correlation between surface charge density and photoluminescence intensity, as demonstrated by successive particle surface deprotonation. As the mechanism is based on anion adsorption, this phenomenon may be transferrable to the specific adsorption of ions, which is relevant for optical sensing. Furthermore, a suitable concentration technique, e.g., by adsorbing those particles on support materials could aid in harvesting their unique optical properties in different applications. One example is the field of scintillation, where the short emission lifetime of the cluster composed of a material with a large atomic number (gold atoms) makes them particularly attractive. In advanced medical imaging technologies, fast scintillators are required to achieve high-resolution imaging at the millimeter length scale.^[62] This supporting procedure of inorganic Au NC also leads to excellent model material for heterogeneous catalysis, which benefits from the high specific surface area of the inorganic metal NC as well as from their high surface charge.^[63] Synthesis of

supported catalysts from laser-based synthesis routes was already demonstrated to be scalable to kilograms of catalysts for larger noble metal NPs^[64] and transferability to Au NC with higher specific surface areas could be highly interesting. Note that surface charge tuning of ligand-free, laser-generated Au NCs has recently been demonstrated as an approach to understand the role of surface charge and size in heterogeneous catalysis of gold clusters supported on titania, evaluated for four different oxidation catalytic reactions.^[41] Here, naked Au NCs are in general beneficial as no energy-intensive calcination to remove ligands is required, which could cause particle ripening and aggregation and impede catalytic activity.

4. Experimental Section

Synthesis: Laser-generated Au NPs with an average particle diameter of 53 nm were used as the educt of the fragmentation process. These particles were synthesized via laser ablation in liquids (LAL) following a protocol described in ref. [27]. In short, LAL was performed using a picosecond-pulsed Nd:YAG laser (Ekspla, Atlantic Series, 10 ps, 1064 nm, 8.8 mJ, 100 kHz, 10 min) in an ablation chamber filled with 30 mL deionized water and subsequent centrifugation ($73 \times g$, 90 min), and then the colloidal particles were separated from the pellet. The gold concentration after centrifugation was 150 mg L^{-1} and was diluted to 7.5 mg L^{-1} for the fragmentation procedure. The LFL was conducted with a nanosecond laser (Innolas, Spitlight, 9 ns, 100 Hz, 84 mJ, 532 nm) in a free liquid jet reactor. The thickness of the fluid jet was 1.1 mm. The laser beam was focused by a cylindrical lens. LFL was conducted in front of the geometrical focus of the lens at a fluence of 1.5 J cm^{-2} . Each experiment included four irradiation cycles (passages).

Colloid Characterization: The NPs generated by LAL were analyzed by UV–vis extinction spectroscopy (Thermo Scientific, Evolution 201) and analytical disc centrifugation (ADC, CPS Instruments DC 24000, 24 000 rpm). The separation of the Au NCs from the remaining colloid after the fragmentation was done by ultrafiltration (1145 g, 20 min) at pH 9.5 (changed using NaOH) with centrifugal filters (Amicon Ultra, Z648000-8EA, 50 kDa). The resulting Au NCs were characterized by UV–vis extinction spectroscopy (Thermo Scientific, Evolution 201) and fluorescence spectroscopy (Varian Eclipse) at a constant mass concentration of dispersed Au NCs of 1.5 mg L^{-1} . The zeta potential was recorded with a Zetasizer (Malvern, Nano ZS) at different pH values (changed using NaOH or HCl). The surface charge density was evaluated from the zeta potential. Due to the low ionic strengths and small particle sizes, the Hückel model was used for the conversion of electrophoretic mobilities into zeta potentials.^[65] The mass of the NCs was determined by inductively coupled plasma mass spectrometry (ICP-MS, Perkin Elmer Sciex - ELAN 6000). Their diameters and crystal structures were identified by TEM (Zeiss EM 910 and JEM 2200FS) by either measuring the particle size or performing a fast Fourier transformation. Additionally, AUC (Beckmann Coulter, optima XLI) was performed, which gave access to the hydrodynamic particle diameter. Measurements were performed in the sedimentation-velocity mode under centrifugal field conditions of $11\,290 \times g$, $20 \text{ }^\circ\text{C}$, and 100 scans were performed for each sample. To measure the molecular weight of the particles, nano-ESI was further conducted on a quadrupole time-of-flight mass spectrometer (micro-qTOF, Bruker-Daltonics, Bremen, Germany, mass resolution 10 000). The samples were recorded at a final concentration of $\approx 1 \text{ mg Au mL}^{-1}$. The samples were analyzed in positive and negative ion modes: each data point was the summation of spectra over 5 min. Interestingly, an ion signal was only observed in negative mode. External calibration was carried out with a set of synthetic peptides. The nano-ESI method considerably increased the signal intensity and yielded stable signals at $3 \mu\text{L h}^{-1}$. The molecular weight

distribution was determined by a multiplicative correlation algorithm (MCA). The multiplicative correlation was designed to enhance the deconvoluted signal when the parent molecule was distributed into several charge states in the measured spectrum.^[66] Molecular weight spectra were converted into particle diameter (nm) as described in the Supporting Information.

Quantum Yield Measurement: The QY of the NCs was measured following reported methodology^[67] using an Agilent 8453 UV-visible Spectroscopy System and Horiba Fluorolog-3 instrument. Quinoline sulfate (in 0.1 M H₂SO₄) was chosen as the reference dye with a known QY of 0.54.

Computation Methodology: All ground-state calculations were carried out with the TURBOMOLE 7.3 program package.^[68] The structure optimizations were carried out with a single-zeta basis set with polarization functions on all atoms, def2-SVP,^[69] employing the Perdew–Burke–Ernzerhof generalized-gradient approximation (GGA) exchange–correlation functional,^[70] the COSMO^[51] with parameters for water (dielectric constant: 78.39; radius of solvent: 1.93 Å) to take into account the solvent effects at the single-particle level, using the m4 grid space option for integration. On top of the optimized structures, two-component calculations were carried out using the dhf-SVP-2c basis set^[53,54] with corresponding relativistic effective core potentials for gold and the range-separated wb97X-D exchange–correlation functional.^[50] On top of the two-component calculations, the excitonic states were calculated with the in-house implementation of SCIS, employing bulk screening with an approximate dielectric constant of 9.84 from ref. [71]. The frequency dependence of the dielectric constant (which also accounts for the size dependence) was neglected, employing 16 valence and 16 conduction states (a change of below 0.1 meV in the lowest excitonic state was considered as the convergence criterium for the CI space). It should be noted that such a highly approximate screening model might not be ideal, however, because only one gold nanocluster size was considered, the qualitative trends were expected to be stable with respect to that choice.

Time-Correlated Single-Photon Counting (TCSPC): TCSPC was used to record the time decay profiles. The setup for these measurements is shown in Figure S18 in the Supporting Information. The samples were excited after focusing the laser beam with a fused silica lens on a Suprasil quartz glass cuvette (Hellma Analytics, Germany). The excitation wavelength $\lambda_{\text{ex}} = 254$ nm was obtained from a frequency tripled titanium–sapphire laser (Tsunami, Spectra Physics Lasers Inc., USA) with a pulse width of 1.7 ps and a repetition rate of 80 MHz. A photodiode (PMA-200, PicoQuant, Germany) was used for the trigger signal. A bandpass filter (254/10 Metal-UV ET, AHF analysentechnik AG, Germany) was placed after the flexible harmonic generator (GWU2 23-PS, Spectra Physics Lasers Inc., United States) to ensure that only the tripled frequency (3ω) excites the AuNCs. Selection of the emission wavelength at $\lambda_{\text{em}} = 340$ nm was achieved by using a scanning monochromator with a 1200 g mm⁻¹ grating blazed at 250 nm (2035, McPherson, USA). The monochromator was connected to a hybrid photomultiplier detector assembly (PMA hybrid series 06, PicoQuant, Germany), which is sensitive in the range of 220 to 650 nm. This detector was connected to a single-photon counting PCI express card (TimeHarp260P, PicoQuant, Germany) inside the PC setup. The resolution was 0.025 ns. The maximum laser power was 3.1 mW. An optical density filter, optimized for the UV-range, was used to reduce the power to around 0.3 mW. To analyze the obtained data, the software FluoFit (PicoQuant, Germany) was used. To consider the instrument response function (IRF), a numerical reconvolution algorithm was applied. The IRF (full width at half maximum: 92 ps) was recorded by using a diluted suspension of colloidal silica (Ludox, Sigma-Aldrich).

X-ray Absorption Spectroscopy (XAS): The colloids were adsorbed onto carbon (Vulcan, Cabot Corporation), dried, and pressed into pellets of 3 mm thickness. XAS was performed at the SUL-X beamline of the Karlsruhe Light Source. The X-ray beam around the Au-L(III) edge of about 1 mm × 1 mm size was measured in transmission by a pair of ionization chambers, and X-ray fluorescence emission was recorded on a multielement silicon drift detector (7 element SiriusSD, Rayspec

with Falcon electronics, XIA). After standard corrections, both spectra matched well. The near-edge structure (XANES) provided information on the lowest unoccupied electronic states, as well as symmetry-related selection rules. Spectra were compared to reference compounds (gold foil, aqueous gold (III) chlorate HAuCl₄, and CTAB-bound monovalent gold, CTAB: cetyl triammoniumbromide), according to established procedures.^[72] In the extended absorption spectrum (EXAFS), emitted electrons probed the next neighbors to reveal information on atomic correlations in the cluster using Fourier inversion as described in the Supporting Information.

Supporting Information

Supporting Information is available from the Wiley Online Library or from the author.

Acknowledgements

The authors gratefully acknowledge the Deutsche Forschungsgemeinschaft (DFG) for its financial support under Project Nos. BA 3580/22-1 and PA 794/28-1. B.G.-L. gratefully acknowledges the Bundesministerium für Bildung und Forschung (BMBF) for funding under project 05K19GU5. The authors also thank Jurij Jacobi and Dr. Marcus Heidelmann for their experimental support in producing the HR-TEM images.

Open access funding enabled and organized by Projekt DEAL.

Conflict of Interest

The authors declare no conflict of interest.

Data Availability Statement

The data that support the findings of this study are available from the corresponding author upon reasonable request.

Keywords

core effect, density functional theory, ligand-free Au nanoclusters, origin of Au nanocluster fluorescence, surface charge, surface effect, ultrasmall gold nanoparticles

Received: February 24, 2021

Revised: April 8, 2021

Published online:

- [1] I. Chakraborty, T. Pradeep, *Chem. Rev.* **2017**, *117*, 8208.
- [2] R. Jin, C. Zeng, M. Zhou, Y. Chen, *Chem. Rev.* **2016**, *116*, 10346.
- [3] T. Huang, R. W. Murray, *J. Phys. Chem. B* **2001**, *105*, 12498.
- [4] H. Liu, G. Hong, Z. Luo, J. Chen, J. Chang, M. Gong, H. He, J. Yang, X. Yuan, L. Li, X. Mu, J. Wang, W. Mi, J. Luo, J. Xie, X.-D. Zhang, *Adv. Mater.* **2019**, *31*, 1901015.
- [5] a) D. Shen, M. Henry, V. Trouillet, C. Comby-Zerbino, F. Bertorelle, L. Sancey, R. Antoine, J.-L. Coll, V. Josserand, X. Le Guével, *APL Mater.* **2017**, *5*, 053404; b) W.-F. Lai, W.-T. Wong, A. L. Rogach, *Adv. Mater.* **2020**, *32*, 1906872; c) C. N. Loynachan, A. P. Soleimany, J. S. Dudani, Y. Lin, A. Najer, A. Bekdemir, Q. Chen, S. N. Bhatia, M. M. Stevens, *Nat. Nanotechnol.* **2019**, *14*, 883.

- [6] Y. Liu, K. Ai, X. Cheng, L. Huo, L. Lu, *Adv. Funct. Mater.* **2010**, *20*, 951.
- [7] T. Higaki, Y. Li, S. Zhao, Q. Li, S. Li, X.-S. Du, S. Yang, J. Chai, R. Jin, *Angew. Chem., Int. Ed.* **2019**, *58*, 8291.
- [8] M.-M. Shi, Di Bao, B.-R. Wulan, Y.-H. Li, Y.-F. Zhang, J.-M. Yan, Q. Jiang, *Adv. Mater.* **2017**, *29*, 1606550.
- [9] a) N. A. Sakthivel, M. Shabaninezhad, L. Sementa, B. Yoon, M. Stener, R. L. Whetten, G. Ramakrishna, A. Fortunelli, U. Landman, A. Dass, *J. Am. Chem. Soc.* **2020**, *142*, 15799; b) H. Kawasaki, K. Hamaguchi, I. Osaka, R. Arakawa, *Adv. Funct. Mater.* **2011**, *21*, 3508.
- [10] C. Helmbrecht, D. Lützenkirchen-Hecht, W. Frank, *Nanoscale* **2015**, *7*, 4978
- [11] a) M. Eichelbaum, K. Rademann, A. Hoell, D. M. Tatchev, W. Weigel, R. Stöber, G. Pacchioni, *Nanotechnology* **2008**, *19*, 135701; b) X. Le Guével, B. Hötzer, G. Jung, K. Hollemeyer, V. Trouillet, M. Schneider, *J. Phys. Chem. C* **2011**, *115*, 10955; c) K. Lemke, C. Prietzel, J. Koetz, *J. Colloid Interface Sci.* **2013**, *394*, 141; d) F. Bertorelle, C. Moulin, A. Soleilhac, C. Comby-Zerbino, P. Dugourd, I. Russier-Antoine, P.-F. Brevet, R. Antoine, *ChemPhysChem* **2018**, *19*, 165.
- [12] a) L. D'Souza, M. Noeske, R. M. Richards, U. Kortz, *J. Colloid Interface Sci.* **2013**, *394*, 157; b) M. Farrag, M. Tschurl, U. Heiz, *Chem. Mater.* **2013**, *25*, 862; c) K. Kimura, N. Sugimoto, S. Sato, H. Yao, Y. Negishi, T. Tsukuda, *J. Phys. Chem. C* **2009**, *113*, 14076; d) Y. Negishi, Y. Takasugi, S. Sato, H. Yao, K. Kimura, T. Tsukuda, *J. Am. Chem. Soc.* **2004**, *126*, 6518; e) J. Polte, X. Tuae, M. Wuthschick, A. Fischer, A. F. Thuenemann, K. Rademann, R. Kraehnert, F. Emmerling, *ACS Nano* **2012**, *6*, 5791; f) H. Qian, M. Zhu, Z. Wu, R. Jin, *Acc. Chem. Res.* **2012**, *45*, 1470; g) X. Kang, H. Chong, M. Zhu, *Nanoscale* **2018**, *10*, 10758.
- [13] a) S. Link, A. Beeby, S. FitzGerald, M. A. El-Sayed, T. G. Schaaff, R. L. Whetten, *J. Phys. Chem. B* **2002**, *106*, 3410; b) J. Zheng, P. R. Nicovich, R. M. Dickson, *Annu. Rev. Phys. Chem.* **2007**, *58*, 409.
- [14] T.-Q. Yang, B. Peng, B.-Q. Shan, Y.-X. Zong, J.-G. Jiang, P. Wu, K. Zhang, *J. Nanomater.* **2020**, *10*, 261.
- [15] Z. Wu, R. Jin, *Nano Lett.* **2010**, *10*, 2568.
- [16] V. Bonačić-Koutecký, R. Antoine, *Nanoscale* **2019**, *11*, 12436.
- [17] J. Zheng, C. Zhou, M. Yu, J. Liu, *Nanoscale* **2012**, *4*, 4073.
- [18] J. Jiang, C. V. Conroy, M. M. Kvetny, G. J. Lake, J. W. Padelford, T. Ahuja, G. Wang, *J. Phys. Chem. C* **2014**, *118*, 20680.
- [19] C. Zhou, C. Sun, M. Yu, Y. Qin, J. Wang, M. Kim, J. Zheng, *J. Phys. Chem. C* **2010**, *114*, 7727.
- [20] S.-H. Cha, J.-U. Kim, K.-H. Kim, J.-C. Lee, *Chem. Mater.* **2007**, *19*, 6297.
- [21] C. Zhou, J. Yu, Y. Qin, J. Zheng, *Nanoscale* **2012**, *4*, 4228.
- [22] E. M. Goldys, M. A. Sobhan, *Adv. Funct. Mater.* **2012**, *22*, 1906.
- [23] J. A. Lopez-Sanchez, N. Dimitratos, C. Hammond, G. L. Brett, L. Kesavan, S. White, P. Miedziak, R. Tiruvalam, R. L. Jenkins, A. F. Carley, D. Knight, C. J. Kiely, G. J. Hutchings, *Nat. Chem.* **2011**, *3*, 551.
- [24] P. Londoño-Larrea, J. P. Vanegas, D. Cuaran-Acosta, E. Zaballos-García, J. Pérez-Prieto, *Chem. - Eur. J.* **2017**, *23*, 8137.
- [25] J. M. J. Santillán, D. Muñeton Arboleda, D. Muraca, D. C. Schinca, L. B. Scaffardi, *Sci. Rep.* **2020**, *10*, 8217.
- [26] J. M. J. Santillán, D. M. Arboleda, D. Muraca, D. C. Schinca, L. B. Scaffardi, *J. Nanotechnol. Nanomater.* **2020**, *1*, 65.
- [27] A. R. Zieffuß, S. Reichenberger, C. Rehbock, I. Chakraborty, M. Gharib, W. J. Parak, S. Barcikowski, *J. Phys. Chem. C* **2018**, *122*, 22125.
- [28] a) A. R. Zieffuß, S. Barcikowski, C. Rehbock, *Langmuir* **2019**, *35*, 6630; b) M. Lau, I. Haxhij, P. Wägener, R. Intartaglia, F. Brandi, J. Nakamura, S. Barcikowski, *Chem. Phys. Lett.* **2014**, *610–611*, 256.
- [29] A. R. Zieffuß, S. Reich, S. Reichenberger, M. Levantino, A. Plech, *Phys. Chem. Chem. Phys.* **2020**, *22*, 4993.
- [30] A. Kanitz, M.-R. Kalus, E. L. Gurevich, A. Ostendorf, S. Barcikowski, D. Amans, *Appl. Surf. Sci.* **2019**, *28*, 103001.
- [31] a) L. Delfour, T. E. Itina, *J. Phys. Chem. C* **2015**, *119*, 13893; b) S. Hashimoto, D. Werner, T. Uwada, *J. Photochem. Photobiol., C* **2012**, *13*, 28; c) A. Pyatenko, M. Yamaguchi, M. Suzuki, *J. Phys. Chem. C* **2009**, *113*, 9078; d) K. Yamada, Y. Tokumoto, T. Nagata, F. Mafuné, *J. Phys. Chem. B* **2006**, *110*, 11751.
- [32] F. Naz, V. Koul, A. Srivastava, Y. K. Gupta, A. K. Dinda, *J. Drug Targeting* **2016**, *24*, 720.
- [33] M. Zhou, C. Zeng, Y. Chen, S. Zhao, M. Y. Sfeir, M. Zhu, R. Jin, *Nat. Commun.* **2016**, *7*, 13240.
- [34] L. B. Scaffardi, J. O. Tocho, *Nanotechnology* **2006**, *17*, 1309.
- [35] R. Jin, *Nanoscale* **2010**, *2*, 343.
- [36] G. Schmid, B. Corain, *Eur. J. Inorg. Chem.* **2003**, *2003*, 3081.
- [37] a) A. Mooradian, *Phys. Rev. Lett.* **1969**, *22*, 185; b) L. Shang, S. Brandholt, F. Stockmar, V. Trouillet, M. Bruns, G. U. Nienhaus, *Small* **2012**, *8*, 661.
- [38] D. Bain, S. Maity, B. Paramanik, A. Patra, *ACS Sustainable Chem. Eng.* **2018**, *6*, 2334.
- [39] V. Merk, C. Rehbock, F. Becker, U. Hagemann, H. Nienhaus, S. Barcikowski, *Langmuir* **2014**, *30*, 4213.
- [40] J.-P. Sylvestre, A. V. Kabashin, E. Sacher, M. Meunier, J. H. T. Luong, *J. Am. Chem. Soc.* **2004**, *126*, 7176.
- [41] A. R. Zieffuß, I. Haxhij, S. Müller, M. Gharib, O. Gridina, C. Rehbock, I. Chakraborty, B. Peng, M. Muhler, W. J. Parak, S. Barcikowski, S. Reichenberger, *J. Phys. Chem. C* **2020**, *124*, 20981.
- [42] C. Pfeiffer, C. Rehbock, D. Hühn, C. Carrillo-Carrion, D. J. de Aberasturi, V. Merk, S. Barcikowski, W. J. Parak, *J. R. Soc., Interface* **2014**, *11*, 20130931.
- [43] K. Makino, H. Ohshima, *Langmuir* **2010**, *26*, 18016.
- [44] Y. Bao, C. Zhong, D. M. Vu, J. P. Temirov, R. B. Dyer, J. S. Martinez, *J. Phys. Chem. C* **2007**, *111*, 12194.
- [45] a) A. Tahmasbi Rad, Y. Bao, H.-S. Jang, Y. Xia, H. Sharma, E. E. Dormidontova, J. Zhao, J. Arora, V. T. John, B. Z. Tang, T. Dainese, A. Hariri, J. V. Jokerst, F. Maran, M. Y. P. E. Nieh, *Adv. Funct. Mater.* **2021**, *31*, 2009750; b) M.-M. Zhang, K. Li, S.-Q. Zang, *Adv. Opt. Mater.* **2020**, *8*, 1902152.
- [46] a) Y. Ling, J. J. Wu, Z. F. Gao, N. B. Li, H. Q. Luo, *J. Phys. Chem. C* **2015**, *119*, 27173; b) I. Diez, H. Jiang, R. H. A. Ras, *ChemPhysChem* **2010**, *11*, 3100.
- [47] M. D. Scanlon, P. Peljo, M. A. Méndez, E. Smirnov, H. H. Girault, *Chem. Sci.* **2015**, *6*, 2705.
- [48] E. Rosenkrantz, S. Arnon, *Opt. Lett.* **2010**, *35*, 1178.
- [49] P. Avouris, B. N. J. Persson, *J. Phys. Chem.* **1984**, *88*, 837.
- [50] J.-D. Chai, M. Head-Gordon, *Phys. Chem. Chem. Phys.* **2008**, *10*, 6615.
- [51] A. Klamt, G. Schüürmann, *J. Chem. Soc.* **1993**, *2*, 799.
- [52] a) A. Klamt, *J. Phys. Chem.* **1995**, *99*, 2224; b) A. Klamt, V. Jonas, *J. Chem. Phys.* **1996**, *105*, 9972.
- [53] F. Weigend, A. Baldes, *J. Chem. Phys.* **2010**, *133*, 174102.
- [54] D. Figgen, G. Rauhut, M. Dolg, H. Stoll, *Chem. Phys.* **2005**, *311*, 227.
- [55] a) A. Franceschetti, H. Fu, L. W. Wang, A. Zunger, *Phys. Rev. B* **1999**, *60*, 1819; b) G. Bester, *J. Phys.: Condens. Mater.* **2009**, *21*, 023202.
- [56] G. W. Spitznagel, T. Clark, J. Chandrasekhar, P. V. R. Schleyer, *J. Comput. Chem.* **1982**, *3*, 363.
- [57] M. Kasha, *Discuss. Faraday Soc.* **1950**, *9*, 14.
- [58] H. Duggal, P. Rajput, I. Alperovich, T. Asanova, D. Mehta, S. N. Jha, S. Gautam, *Vacuum* **2020**, *176*, 109294.
- [59] M. Hesari, M. S. Workentin, Z. Ding, *ACS Nano* **2014**, *8*, 8543.
- [60] J. Zheng, C. Zhang, R. M. Dickson, *Phys. Rev. Lett.* **2004**, *93*, 77402.
- [61] P. Yu, X. Wen, Y.-R. Toh, X. Ma, J. Tang, *Part. Part. Syst. Charact.* **2015**, *32*, 142.
- [62] R. M. Turtos, S. Gundacker, S. Omelkov, B. Mahler, A. H. Khan, J. Saaring, Z. Meng, A. Vasil'ev, C. Dujardin, M. Kirm, I. Moreels, E. Auffray, P. Lecoq, *npj 2D Mater. Appl.* **2019**, *3*, 37.

- [63] S. Reichenberger, G. Marzun, M. Muhler, S. Barcikowski, *ChemCatChem* **2019**, *11*, 4489.
- [64] S. Dittrich, S. Kohsakowski, B. Wittek, C. Hengst, B. Gökce, S. Barcikowski, S. Reichenberger, *Nanomaterials* **2020**, *10*, 1582.
- [65] T. L. Doane, C.-H. Chuang, R. J. Hill, C. Burda, *Acc. Chem. Res.* **2012**, *45*, 317.
- [66] M. Waszkielewicz, J. Olesiak-Banska, C. Comby-Zerbino, F. Bertorelle, X. Dagany, A. K. Bansal, M. T. Sajjad, I. D. W. Samuel, Z. Sanader, M. Rozycka, M. Wojtas, K. Matczyszyn, V. Bonacic-Koutecky, R. Antoine, A. Ozyhar, M. Samoc, *Nanoscale* **2018**, *10*, 11335.
- [67] J. Hühn, C. Carrillo-Carrion, M. G. Soliman, C. Pfeiffer, D. Valdeperez, A. Masood, I. Chakraborty, L. Zhu, M. Gallego, Z. Yue, M. Carril, N. Feliu, A. Escudero, A. M. Alkilany, B. Pelaz, P. del Pino, W. J. Parak, *Chem. Mater.* **2017**, *29*, 399.
- [68] TURBOMOLE V7.3 2018, a development of University of Karlsruhe and Forschungszentrum Karlsruhe GmbH, 1989–2007, TURBOMOLE GmbH, since 2007; available from <https://www.turbomole.com> (accessed: May 2021).
- [69] a) D. Andrae, U. Huermann, M. Dolg, H. Stoll, H. Preu, *Theor. Chim. Acta* **1990**, *77*, 123; b) F. Weigend, R. Ahlrichs, *Phys. Chem. Chem. Phys.* **2005**, *7*, 3297.
- [70] a) J. P. Perdew, K. Burke, M. Ernzerhof, *Phys. Rev. Lett.* **1996**, *77*, 3865; b) J. P. Perdew, Y. Wang, *Phys. Rev. B* **1992**, *45*, 13244; c) P. A. M. Dirac, *Proc. R. Soc. London, Ser. A* **1929**, *123*, 714; d) J. C. Slater, *Phys. Rev.* **1951**, *81*, 385.
- [71] A. Derkachova, K. Kolwas, I. Demchenko, *Plasmonics* **2016**, *11*, 941.
- [72] B. Abécassis, F. Testard, Q. Kong, B. Francois, O. Spalla, *Langmuir* **2010**, *26*, 13847.